

## Semi-microscopic calculations of the fusion barrier distributions for reactions involving deformed target nuclei

I. I. Gontchar,\* D. J. Hinde, M. Dasgupta, C. R. Morton, and J. O. Newton  
*Department of Nuclear Physics, Research School of Physical Sciences and Engineering,  
 Australian National University, Canberra, ACT 0200, Australia*  
 (Received 19 August 2005; published 21 March 2006)

The double-folding model with an M3Y effective nucleon-nucleon ( $NN$ ) interaction was applied to obtain the angle-dependent bare nucleus-nucleus potential for heavy-ion fusion reactions involving deformed target nuclei. The angular dependence with a zero-range exchange  $NN$  interaction is almost identical to that with a finite-range interaction, allowing quick calculations of the fusion cross sections and corresponding barrier distributions  $D(E_{c.m.})$ . Since in the literature the experimental  $D(E_{c.m.})$  have been analyzed usually using a Woods-Saxon shape for the nuclear part of the nucleus-nucleus potential, we fitted the spherical double-folding potentials at the barrier radii with a Woods-Saxon (WS) form. The calculated  $D(E_{c.m.})$  with this fitted WS potential, but now accounting for the deformation of the target nuclei, are significantly different from the  $D(E_{c.m.})$  calculated directly using the double-folding potential. This indicates that the finite size effects are substantial and should not be ignored in the analysis of experimental fusion cross sections and barrier distributions for reactions with statically deformed nuclei.

DOI: [10.1103/PhysRevC.73.034610](https://doi.org/10.1103/PhysRevC.73.034610)

PACS number(s): 24.10.-i, 25.70.Jj

### I. INTRODUCTION

In heavy-ion fusion reactions involving heavy, statically deformed nuclei, it has long been recognized [1] that a distribution of fusion barrier energies arises from random orientations of the target nuclei. In 1991, it was shown [2] that the actual distribution of probabilities for finding a fusion barrier at a given center-of-mass energy  $E_{c.m.}$  [called the experimental fusion barrier distribution  $D(E_{c.m.})$ ] could be directly extracted from precise experimental fusion cross sections  $\sigma$  by double differentiation of  $E\sigma$  with respect to energy:

$$D(E_{c.m.}) = \frac{d^2(E_{c.m.}\sigma)}{dE_{c.m.}^2}. \quad (1)$$

Calculations show that different nuclear shapes result in different barrier distributions. Although differentiating experimental data twice demanded a new level of experimental precision, soon experimental barrier distributions were measured [3] for reactions involving heavy, statically deformed nuclei. These demonstrated that measurements of  $D(E_{c.m.})$  can give information on the magnitude and sign of the static nuclear deformation parameters [4], at least up to  $\beta_4$ . In principle, a heavy-ion projectile should be a sensitive probe of static deformation, because of the short wavelength. Thus, the possibility of measuring static deformations from experimental heavy-ion fusion barrier distributions was a topic of discussion, and investigations of the sensitivity of barrier distributions even to  $\beta_6$  were carried out [5]. However, as measurements of  $D(E_{c.m.})$  for reactions with statically deformed nuclei increased in number, it was found that calculations of  $D(E_{c.m.})$  using deformation parameters from

the literature generally did not result in completely satisfactory reproduction of the measurements [6,7].

In these analyses, the calculated  $D(E_{c.m.})$  were obtained from a geometrical model, generally using the computer code CCDEF and its daughter CCMOD, which include an angle-dependent Woods-Saxon form for the nuclear contribution to the nucleus-nucleus potential:

$$U_{nWS} = - \frac{V_{WS}}{1 + \exp \left\{ \left[ R - r_{WS} (A_P^{1/3} + A_T^{1/3} f(\theta)) \right] / a_{WS} \right\}}. \quad (2)$$

Here  $V_{WS}$ ,  $r_{WS}$ , and  $a_{WS}$  are the depth, radius, and diffuseness parameters of the potential, and  $\theta$  is the angle between the symmetry axis of the target nucleus and the beam direction.  $R$  denotes the distance between the centers of mass of the projectile nucleus of mass number  $A_P$  and the target nucleus of mass number  $A_T$ . In the function  $f(\theta)$  defining the target deformation, multipoles up to sixth order have been included:

$$f(\theta) = \lambda^{-1} [1 + \beta_2 Y_{20}(\theta) + \beta_4 Y_{40}(\theta) + \beta_6 Y_{60}(\theta)]. \quad (3)$$

Here  $\lambda$  guarantees volume conservation [8].

However, this approach neglected at least two physical effects that may be important. Firstly,  $U_{nWS}$  was determined along the line joining the centers of the two nuclei (which we call the center-line potential), whereas for deformed nuclei interacting with a finite size projectile, this does not usually correspond to the minimum distance between the nuclear surfaces. Secondly, the expectation of a dependence of the nuclear potential on the surface curvature was disregarded. It was shown geometrically in Ref. [9] that these two effects can significantly change the calculated near-barrier fusion cross sections and, thus, the corresponding  $D(E_{c.m.})$ .

If the nuclear part of the nucleus-nucleus potential were calculated by means of a semi-microscopic double-folding model (DFM), all such finite size and curvature effects should be automatically accounted for. The DFM was applied in

\*Permanent address: Omsk State Transport University, pr. Marxa 35, Omsk RU-644046, Russia.

Ref. [10] to calculate the fusion barrier energies for reactions where both projectile and target nuclei are spherical. This paper describes the extension of the DFM approach to reactions where the heavy nucleus possesses a static deformation.

The present study has two aims. The first and principal objective of our study is to see how the finite size effects calculated with the DFM compare with those determined geometrically, and how the calculated  $D(E_{c.m.})$  differ from those using the simple center-line Woods-Saxon potential that is widely used. These questions, to our knowledge, are investigated here for the first time. Secondly, it is interesting to see to what extent the DFM can describe the measured  $D(E_{c.m.})$ . This question was already addressed in Ref. [11] where, however, calculations had been made for only one reaction ( $^{16}\text{O} + ^{154}\text{Sm}$ ) accounting for quadrupole and hexadecapole deformations of  $^{154}\text{Sm}$ . There, the calculated  $D(E_{c.m.})$  exhibited a double-humped structure (see Fig. 6 of Ref. [11]) that is not observed in experiment and was not explained in that work. We will compare our results with those of Ref. [11] and with a number of experimental barrier distributions.

The basic equations of the DFM can be found in many papers; see e.g., Refs. [12] and [13]. Recently a new computer code was developed, as described in Ref. [10], to calculate the DFM nucleus-nucleus potential for the interaction of two spherical nuclei. All the basic equations of the DFM are presented in that paper.

Aspects of the DFM as applied to deformed target nuclei are described in Refs. [14] and [11]. However, in order to make this paper self-contained, we describe in Sec. II the extensions made to the code of Ref. [10] to allow modeling of collisions of deformed nuclei, including the choice of the input parameters for the DFM calculations that are compared to experimental data. We also make a comparison between the fusion barrier energies calculated using the zero- and finite-range exchange term of the M3Y  $NN$  interaction and show that the time-consuming finite-range calculations can be well reproduced by much faster zero-range calculations. Section III is devoted to the comparison of the calculations with experimental fusion barrier distributions, and with other calculations not using the DFM.

## II. DOUBLE-FOLDING MODEL FOR FUSION WITH STATICALLY DEFORMED NUCLEI

### A. Formalism

The geometry of the collision of a spherical projectile nucleus  $P$  with a deformed but axially symmetric target nucleus  $T$  is illustrated in Fig. 1. The interaction potential between the two nuclei reads

$$U_{PT}(\mathbf{R}) = U_C(\mathbf{R}) + U_n(\mathbf{R}) + \frac{\hbar^2 L(L+1)}{2\mu R^2}. \quad (4)$$

Here the electrostatic (Coulomb) interaction energy  $U_C(\mathbf{R})$  and the nuclear interaction energy  $U_n(\mathbf{R})$  are defined by Eqs. (5)–(7) of Ref. [10] in which, however,  $R$  must be replaced by  $\mathbf{R}$ . An important point is that the nucleus-nucleus potential and its Coulomb and nuclear components depend not only on the center-to-center distance  $R$  but also on the angle  $\theta$  between the center-to-center line and the symmetry axis of the deformed

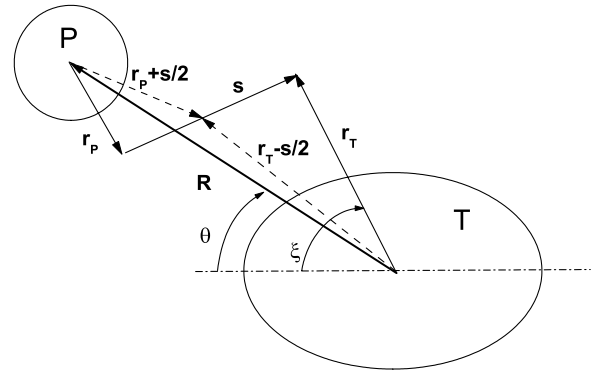


FIG. 1. Coordinate system used in the double-folding model. Vector between the centers of the projectile  $P$  and target  $T$  nuclei is denoted by  $\mathbf{R}$ , while  $\mathbf{r}_p, \mathbf{r}_t$  are the radius vectors of points separated by  $\mathbf{s}$  in the nucleon distributions of the projectile and target nuclei. To calculate the nucleus-nucleus potential as a function of  $R$  and  $\theta$ , integration with respect to angle  $\xi$  must be performed.

nucleus. The last (centrifugal) term is written as normal in the point-particle approximation. By absorbing the centrifugal kinetic energy into the potential, it is implicitly assumed that the two nuclei approach on radial trajectories for all angular momenta. This assumption may lead to geometrical errors for large angular momenta; however, this aspect of fusion with deformed nuclei is beyond the scope of this paper, where we concentrate on the barrier distribution, involving only low angular momenta.

The nuclear part of the potential  $U_n$  consists of two terms, the direct  $U_{nD}$  term and the exchange  $U_{nE}$  term. The direct part of the interaction between two colliding nuclei and the equation describing the Coulomb interaction have similar forms [see Eqs. (5) and (6) of Ref. [10]] involving only diagonal elements of the density matrix. The exchange part involves nondiagonal elements of the density matrix and the wave number  $k_{\text{rel}}(\mathbf{R})$  associated with the relative motion of the colliding nuclei. Here again it is significant that the  $k_{\text{rel}}$  depends on both the center-to-center distance and the mutual orientation of the target and projectile nuclei.

Two parametrizations of the effective nucleon-nucleon interaction in the literature are those of the Reid [15] and Paris [16] interactions. Since they are not significantly different [16] and result in very similar barrier energies in the case of spherical reactants [10], we consider in this work only the Paris M3Y effective interaction. Both the direct  $v_D$  and the exchange  $v_{Ef}$  parts of the  $NN$  interactions comprise a sum of Yukawa-type terms [see Eqs. (9) and (10) of Ref. [10]]. Here, subscript  $D$  refers to the direct part of the  $NN$  interaction, while the subscript  $Ef$  refers to the finite-range exchange part of the  $NN$  interaction. Instead of a finite-range exchange  $NN$  interaction, one of zero range was used in early work [17]:  $v_{E\delta}(\mathbf{s}) = G_{E\delta}\delta(\mathbf{s})$ . The values of all the coefficients of the  $NN$  interaction are collected in Table I of Ref. [10]. Unless specified otherwise, these values are used throughout this paper.

In Ref. [18], it was shown that the original density-independent M3Y interaction failed to saturate cold nuclear matter. In order to obtain the correct value of the central nucleon density and binding energy, several versions of a

density-dependent M3Y interaction have been proposed (see, e.g., Refs. [18] and [19]). The density dependence enters as a multiplier  $F(\rho_{FA})$  of the density-independent  $NN$  interaction. The function  $F$  is given by Eq. (12) of Ref. [10] where the nucleon density  $\rho_{FA}$  is specified as well. The density-dependent Paris  $NN$  interaction results in the correct saturation binding energy of about 16 MeV/nucleon and a nuclear density of  $0.17 \text{ fm}^{-3}$ , for several sets of coefficients that are presented in Table I of Ref. [19] and Table II of Ref. [10]. The use of a density-dependent  $NN$  interaction means that the bare M3Y direct and exchange  $NN$  interactions,  $v_D(s)$  and  $v_{Ef}(s)$ , in the folding integrals should be replaced by products  $F(\rho_{FA})v_{D(Ef)}(s)$ .

### B. Evaluating the double-folding integrals

If a zero-range exchange interaction is used, the nondiagonal elements of the density matrix in the folding integral are reduced to diagonal elements. The resulting integral can be easily evaluated. However, when a finite-range exchange interaction is applied, three factors cause major difficulties in calculating the exchange part of the nuclear potential.

First,  $k_{\text{rel}}$ , which should be known to find the nucleus-nucleus interaction potential  $U_{PT}(\mathbf{R})$ , depends on the interaction potential, resulting in a self-consistency problem. It is overcome by applying an iterative procedure [10].

Second,  $k_{\text{rel}}$  depends on the initial energy of relative motion  $E_{\text{c.m.}}$ . It is technically impractical to calculate the double-folding integrals for each individual value of  $E_{\text{c.m.}}$ . Fortunately,  $U_{PT}(R, \theta)$  depends rather weakly upon  $E_{\text{c.m.}}$  via  $k_{\text{rel}}$ . Therefore, we calculate the  $U_{PT}(R, \theta)$  for  $E_{\text{c.m.}} = B_Z = Z_P Z_T / (A_P^{1/3} + A_T^{1/3})$  and use this potential for any value of  $E_{\text{c.m.}}$  around  $B_Z$ .

The third obstacle is much more complicated. In order to compute the integral for the exchange part of the nuclear potential, one has to calculate the nondiagonal elements of the density matrix which depend on two spatial points. The calculation is performed using the density matrix expansion method of Refs. [20] and [21], which makes the following approximation:

$$\rho_A(\mathbf{r}; \mathbf{r} + \mathbf{s}) \simeq \rho_A(\mathbf{r} + \mathbf{s}/2) \hat{j}_1[\mathbf{k}_{\text{eff}}(\mathbf{r} + \mathbf{s}/2) \cdot \mathbf{s}]. \quad (5)$$

Here  $\rho_A$  stands for the matter density distribution of either projectile ( $\rho_{PA}$ ) or target ( $\rho_{TA}$ ) nucleus. The modified Bessel function  $\hat{j}_1$  is presented by Eq. (15) of Ref. [10]. The effective Fermi momentum  $k_{\text{eff}}$  is calculated using the extended Thomas-Fermi approach [21]; see Eq. (16) of Ref. [10]. For the strength of the Weizsäcker correction term  $C_s$ , the value  $1/36$  is used according to Ref. [22].

In practice, when evaluating the double-folding integrals, the momentum-space representation is used. Where only diagonal matrix elements are involved, i.e., for the Coulomb, nuclear direct, and nuclear zero-range exchange energies, the actual formulas used for the computation (closely following Ref. [14]) read

$$U(R, \theta) = \sum_{l=0,2,\dots}^{l_{\text{max}}} U_l(R) Y_{l0}(\theta). \quad (6)$$

In this equation,  $U(R, \theta)$  stands for either  $U_C(R, \theta)$ ,  $U_{nD}(R, \theta)$ , or  $U_{nE}(R, \theta)$ , and

$$U_l(R) = \frac{2}{\pi} \int_0^{k_{\text{max}}} dk k^2 j_l(kR) v(k) B_{lT}(k) B_{0P}(k). \quad (7)$$

Here  $v(k)$  denotes the Fourier transform of either Coulomb, nuclear direct, or nuclear exchange nucleon-nucleon interactions (see Ref. [14] for the relevant equations),  $j_l$  are spherical Bessel functions, and the coefficients  $B_l$  read

$$B_l(k) = \int_0^{r_{\text{max}}} dr r^2 \rho_l(r) j_l(kr). \quad (8)$$

The multipole components of the projectile or target density  $\rho_l$  are defined as

$$\rho_l(r) = 2\pi \int_0^\pi d\xi \sin(\xi) \rho(r, \xi) Y_{l0}(\xi). \quad (9)$$

From these equations, the sixfold integrals are reduced to threefold integrals. Furthermore, the coefficients  $B_l(k)$  need to be prepared only once for a given reaction, thus reducing the computation to the single integration in Eq. (7) for each value of  $R$ . This dramatically reduces computer time.

In the case of a finite-range exchange term in the  $NN$  interaction, computation of the double-folding integral is more involved (here we follow Refs. [12] and [11]). The actual formulas used for the computation read

$$U_{nE}(R, \theta) = 4\pi \int_0^{s_{\text{max}}} ds s^2 j_0(k_{\text{rel}} \cdot s) \times v(s) G(R, s, \theta). \quad (10)$$

$$G(R, s, \theta) = \int_0^\pi d\xi \int_0^{q_{\text{max}}} dq q^2 \sin(\xi) \times h_P(R, s, q, \xi, \theta) h_T(R, s, q, \xi). \quad (11)$$

$$h_T(s, q, \xi) = \rho_T(q, \xi) j_1(k_{T\text{eff}}(q, \xi) \cdot s). \quad (12)$$

$$h_P(R, s, q, \xi, \theta) = \int_0^{2\pi} d\varphi \rho_P(p) j_1(k_{P\text{eff}}(p) \cdot s). \quad (13)$$

$$p(R, q, \xi, \varphi, \theta) = |\mathbf{q} - \mathbf{R}| = [q^2 + R^2 + 2Rq(\sin\theta \sin\xi \cos\varphi - \cos\theta \cos\xi)]^{1/2}. \quad (14)$$

For simplicity, we denoted  $\mathbf{r}_P + \mathbf{s}/2 = \mathbf{p}$  and  $\mathbf{r}_T - \mathbf{s}/2 = \mathbf{q}$  (see Fig. 1).

For the finite-range exchange interaction, the sixfold integral is reduced formally to a fourfold integral described by Eqs. (10), (11), and (13). However, this should be calculated for each pair  $(R, \theta)$ , while the function  $h_P(R, s, q, \xi, \theta)$  can be prepared in advance, but depends on five variables. The computer time needed for the finite-range calculations is roughly 3 orders of magnitude larger than required for the zero-range calculations.

For best performance, the upper limits of the integrals should be optimally set,  $k_{\text{max}}$  [Eq. (7)],  $r_{\text{max}}$  [Eq. (8)],  $s_{\text{max}}$  [Eq. (10)],  $q_{\text{max}}$  [Eq. (11)] and the maximum value of the summation index  $l_{\text{max}}$  [Eq. (6)]. The physical results should not depend upon the actual values of these parameters, but the computations should be reasonably fast. We found that for the reactions under consideration, these conditions are

fulfilled with  $r_{\max} = s_{\max} = q_{\max} = 3R_T$ ,  $k_{\max} = 5 \text{ fm}^{-1}$ , and  $l_{\max} = 10$ . Inclusion of too few multipoles may result in oscillations in the results.

### C. Calculating fusion cross sections and barrier distributions

To calculate the fusion cross sections quantum mechanically, the coupling of the relative motion of the reactants to the rotational states of the deformed target nucleus should be modeled. However, in this work we must apply the commonly used semi-classical approach, which for well-deformed heavy nuclei gives results very close to those of full quantum mechanical calculations (see, e.g., Refs. [5,23]).

The transmission coefficients  $T_L(\theta)$  were calculated using the parabolic barrier approximation, for each value of  $\theta$  in the interval  $0^\circ$  to  $90^\circ$  with a step of  $5^\circ$ . Then the fusion cross sections were found according to the formulas of Refs. [4,23]

$$\sigma(L, \theta) = \frac{\pi \hbar^2}{2\mu E_{c.m.}} \left( \frac{2L + 1}{1 + \exp\{2\pi[V_B - E_{c.m.}]/\hbar\omega_B\}} \right), \quad (15)$$

where  $V_B$  and  $\omega_B$  are both  $L$ - and  $\theta$ -dependent as detailed in Appendix A, and

$$\sigma = \sum_L \sum_i \sigma(L, \theta_i) \sin(\theta_i) \Delta\theta. \quad (16)$$

We found that changing the  $\Delta\theta$  from  $5^\circ$  to  $2^\circ$  or  $1^\circ$  typically changes the cross sections and barrier distributions by less than 2%, indicating that a step of  $5^\circ$  is small enough.

### D. Input parameters for the calculations

The DFM calculations require the following input parameters: the nucleon density distribution for colliding nuclei and the values of the deformation parameters  $\beta_2$ ,  $\beta_4$ , and  $\beta_6$  of the target nucleus. In these calculations, for simplicity we take  $\rho_{P(T)A} = \rho_{P(T)Z}A/Z$ . For the proton density distributions  $\rho_{P(T)Z}$ , two-parameter Fermi (2pF) profiles were used for both

projectile and target nuclei:

$$\rho_{PZ}(r) = \rho_{0P}\{1 + \exp[(r - R_P)/a_P]\}^{-1}, \quad (17)$$

$$\rho_{TZ}(r, \theta) = \rho_{0T}\{1 + \exp[(r - R_T f(\theta))/a_T]\}^{-1}. \quad (18)$$

The parameters  $R_{P(T)}$  and  $a_{P(T)}$  were defined using the data on the charge density obtained experimentally from electron elastic scattering. The values of these parameters as well as their sources are presented in Table I. For those nuclei where the data were not available in the literature, the radius parameters were obtained by scaling those of the closest nuclei. The diffuseness of the charge density was taken to be equal to that of the closest nucleus for which it was available. The influence of the diffuseness of the nucleon (proton) density distribution on the barrier energy has been discussed in Ref. [10].

For four of the five target nuclei in Table I, information on  $R_T$  and  $a_T$  was taken from the electron scattering analysis of Ref. [24]. That study has several advantages. Firstly, the data were fitted with a target charge density profile as given in Eq. (18). Secondly, not only the values of  $R_T$  and  $a_T$  were found, but also the deformation parameters  $\beta_{2,4,6}$ , were obtained at the same time. The sets of parameters from this work are used throughout the paper, if not specified otherwise.

The electron scattering data give information on the charge density distribution of the scattering nucleus, whereas in the DFM the point proton and nucleon density distributions are needed. Therefore, the radius parameters for the proton density were taken to be equal to those for the charge density, whereas the diffuseness parameters were corrected for the finite width of the charge distribution of a single proton. In order to make this correction, we used the relation between the average square radii of the proton and charge distributions. The actual formula relating the diffuseness of the charge distribution  $a_C$  to that of the point proton density distribution  $a_Z$  reads

$$a_Z = \sqrt{a_C^2 - \frac{5\pi^2}{7} \left(0.76 - 0.11 \frac{N}{Z}\right)}, \quad (19)$$

TABLE I. Seven reactions for which calculations of the  $D(E_{c.m.})$  were performed and for which experimental data on the  $D(E_{c.m.})$  are available. Values of the target nucleus deformation parameters  $\beta_{2,4,6}$  and of the matter density distribution parameters of the projectile ( $R_P$  and  $a_P$ ) and target ( $R_T$  and  $a_T$ ) were taken from Ref. [24] unless another source is indicated.

Reaction	$\beta_2$	$\beta_4$	$\beta_6$	$R_P$ (fm)	$a_P$ (fm)	$R_T$ (fm)	$a_T$ (fm)	Source of experimental $D(E_{c.m.})$
$^{16}\text{O} + ^{154}\text{Sm}$	0.311	0.087	-0.018	2.608 <sup>a</sup>	0.465 <sup>a</sup>	5.939	0.479	Ref. [4]
$^{16}\text{O} + ^{186}\text{W}$	0.310 <sup>b</sup>	-0.030 <sup>b</sup>	0.000 <sup>c</sup>	2.608 <sup>a</sup>	0.465 <sup>a</sup>	6.580 <sup>b</sup>	0.433 <sup>b</sup>	Ref. [4]
$^{16}\text{O} + ^{238}\text{U}$	0.261	0.087	0.000	2.608 <sup>a</sup>	0.465 <sup>a</sup>	6.805	0.569	Ref. [6]
$^{34}\text{S} + ^{168}\text{Er}$	0.338 <sup>d</sup>	0.000 <sup>d</sup>	0.025 <sup>d</sup>	3.443 <sup>e</sup>	0.559 <sup>e</sup>	6.161 <sup>f</sup>	0.441 <sup>f</sup>	Ref. [5]
$^{19}\text{F} + ^{232}\text{Th}$	0.238	0.101	0.000	2.580 <sup>g</sup>	0.525 <sup>g</sup>	6.592	0.533	Ref. [27]
$^{12}\text{C} + ^{238}\text{U}$	0.261	0.087	0.000	2.441 <sup>c</sup>	0.456 <sup>c</sup>	6.805	0.569	Ref. [27]
$^{12}\text{C} + ^{232}\text{Th}$	0.238	0.101	0.000	2.441 <sup>c</sup>	0.456 <sup>c</sup>	6.592	0.533	Ref. [7]

<sup>a</sup>Taken from 3pF Ref. [25].

<sup>b</sup>Ref. [26].

<sup>c</sup> $R_P$  was scaled from 3pF  $^{14}\text{N}$ ;  $a_P$  was taken to be the same as for 3pF  $^{14}\text{N}$ , Ref. [25].

<sup>d</sup>Ref. [5].

<sup>e</sup>Ref. [4].

<sup>f</sup>Taken to be the same as in 2pF for  $^{166}\text{Er}$ , Ref. [25].

<sup>g</sup>Taken from 2pF Ref. [25].

as obtained from Eq. (17) of Ref. [17] and the equations relating the average square radius of a 2pF-profile with its radius and diffuseness parameters in Ref. [8].

In the analysis of the electron scattering experiments, the charge diffuseness parameter  $a_T$  was assumed to be angle independent. However, it was pointed out in Ref. [28] that the diffuseness parameter must be angle dependent. This results from the condition that the density gradient normal to a constant density contour should be constant, independent of the deformation. We estimated the effect of the  $a_T$  angular dependence on the barrier distribution and found it to be less than 10% (see Sec. III B for details). To be consistent with previous work [10,11], we took  $a_T$  to be angle independent in all the calculations below unless specifically mentioned.

Having specified the input parameters, we can start to compare the calculated potentials and barrier distributions with other calculations and with experiment. First we compared the fusion barrier energies for reactions of spherical nuclei, as calculated with the new deformed DFM computer code, with the energies obtained using the spherical DFM code developed in Ref. [10]. The barrier energies and radii agreed within 0.05% and 0.2%, respectively. Detailed comparisons with the deformed DFM calculations of Ref. [11] for the reaction of  $^{16}\text{O} + ^{154}\text{Sm}$  are made in Appendix B.

### E. Finite-range versus zero-range exchange interaction: Studying the impact on fusion barrier energies

Our code is able to calculate the nucleus-nucleus potential with both finite-range (including the density dependence of the  $NN$  interaction for the case of two spherical nuclei) and zero-range exchange terms in the M3Y  $NN$  interaction. In Fig. 2, we compare the barrier energies  $V_{B\delta}$  and  $V_{Bf}$  calculated with these two options for the  $^{16}\text{O} + ^{154}\text{Sm}$  reaction, taking  $\beta_{2,4,6} = 0.311, 0, 0$ . In Fig. 3, the same comparison is presented but for  $\beta_{2,4,6} = 0.311, 0.087, -0.018$ . The latter set of deformation parameters were taken from Ref. [24], though the obvious misprinting of  $\beta_6$  was corrected. The barrier energies were calculated as a function of  $\theta$ . We see that changing from zero to finite range practically does not affect the  $V_B(\theta)$  dependence, but rather results in an approximately constant shift downward in energy. Moreover, the shift is very close to that of the spherical case.

Remembering that the finite-range calculations are extremely computer time consuming, we decided to simulate the finite-range calculations by zero-range ones, the latter with a modified strength of the exchange part of the  $NN$  interaction. The modified value of  $G_{E\delta}$  was found by setting the zero-range spherical barrier energy to be equal to that calculated with the finite-range exchange term, whose original value was  $G_{E\delta} = -592 \text{ MeV fm}^3$ . The correction  $\Delta G_{E\delta}$  resulting in reproduction of  $V_{Bf}$  with an accuracy of 0.01 MeV was found to be  $\Delta G_{E\delta} = -160 \text{ MeV fm}^3$  (the zero-range barrier energy is reduced by 0.03 MeV as the  $\Delta G_{E\delta}$  changes by  $10 \text{ MeV fm}^3$ ). Now we calculate the barrier energy  $V_{B\delta m}(\theta)$  with the modified value of  $G_{E\delta} = -752 \text{ MeV fm}^3$ . In the lower panels of Figs. 2 and 3, the differences  $V_{B\delta}(\theta) - V_{Bf}(\theta)$  and  $V_{B\delta}(\theta) - V_{B\delta m}(\theta)$  as well as  $V_{B\delta}(\text{sph}) - V_{Bf}(\text{sph})$  are shown. They differ from each other by  $\sim 0.01 \text{ MeV}$ ,

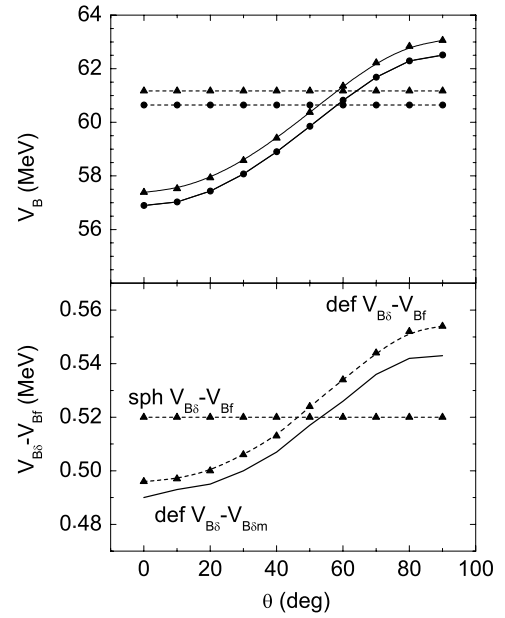


FIG. 2. Upper panel: Barrier energies  $V_{B\delta}$  (lines with triangles) and  $V_{Bf}$  (lines with circles) calculated with the zero- and finite-range exchange interactions, respectively, for  $^{16}\text{O} + ^{154}\text{Sm}$  reaction. Horizontal dashed lines correspond to the spherical target. The curves are for  $\beta_{2,4,6} = 0.311, 0, 0$ . Barrier energies calculated with the modified zero-range exchange interaction,  $V_{B\delta m}$ , are included but are not seen because they practically coincide with the  $V_{Bf}$ . Lower panel: Differences between the barrier energies. Dashed lines indicate  $V_{B\delta} - V_{Bf}$ ; solid line is for  $V_{B\delta} - V_{B\delta m}$ .

essentially independent of angle. Thus, the approximation of the finite-range exchange term by a corrected zero-range exchange term is good enough for our purposes.

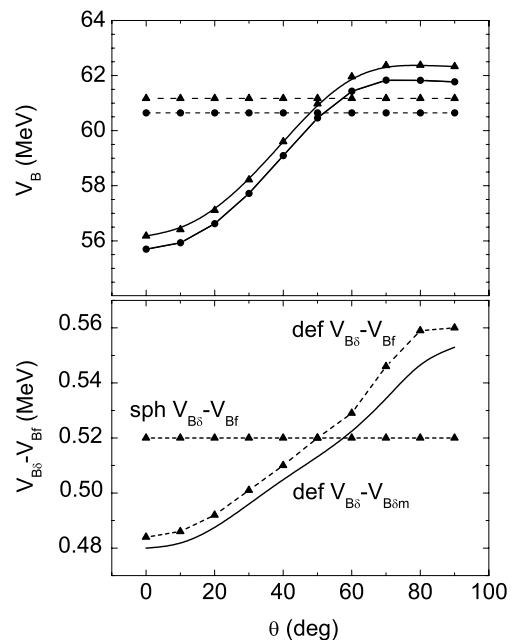


FIG. 3. Same as Fig. 2, but for  $\beta_{2,4,6} = 0.311, 0.087, -0.018$ .

### III. COMPARISON WITH EXPERIMENTAL DATA

The double differentiation to convert the calculated fusion cross sections into the barrier distributions  $D(E_{c.m.})$  was performed according to the same numerical formula used to determine the experimental  $D(E_{c.m.})$  (see Ref. [23]). Moreover, a differentiation step of 2 MeV was used in the calculations, which is also close to those with which the data were processed.

#### A. Reaction $^{16}\text{O} + ^{154}\text{Sm}$

Since many measurements and calculations have focused on the  $^{16}\text{O} + ^{154}\text{Sm}$  reaction [1,3,4,9,11,29,30], we first compare our calculations with the data for this reaction, in Fig. 4. Here the experimental barrier distribution has been evaluated taking an energy step of 2.26 MeV. The calculation shown by the dotted line was made with the unchanged Paris zero-range exchange  $NN$  interaction. The shape of  $D(E_{c.m.})$  is similar to that of the experiment (open circles with the error bars), but the average barrier energy is certainly too high. Figures 2 and 3 show that accounting for the finite range of the exchange interaction reduces the value of  $V_B$ . Therefore, we calculated the  $D(E_{c.m.})$  with an increased strength of the exchange interaction  $\Delta G_{E\delta} = -160 \text{ MeV fm}^3$  (shown by the thin solid line in Fig. 4). This helps, but it is not enough to match the experiment.

An additional reduction in the barrier energy comes from accounting for the density dependence of the  $NN$  interaction as shown in Fig. 5. For simplicity, calculations were done for the  $^{16}\text{O} + ^{154}\text{Sm}$  reaction considering the target nucleus to be spherical. The open circles in this figure correspond to different types of DFM calculations, namely the zero-range ( $\delta$ ) and the finite-range density independent (0) and the density-dependent (1–8) interactions [the coefficients of the function  $F(\rho_{FA})$  are listed in the Table II of Ref. [10]]. The experimentally

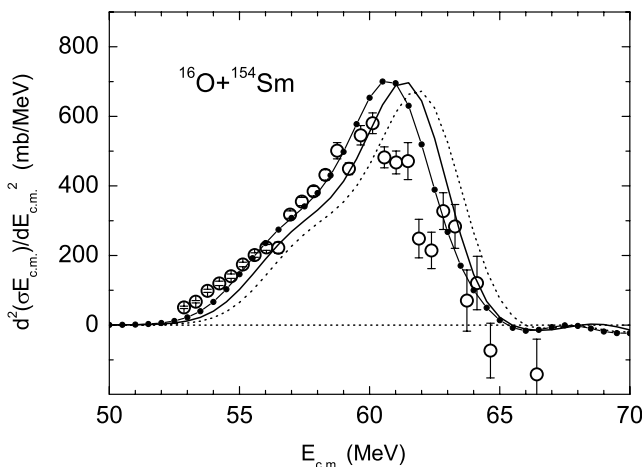


FIG. 4. Barrier distributions defined by Eq. (1) for the  $^{16}\text{O} + ^{154}\text{Sm}$  reaction. Open circles show experimental data of Ref. [4]; lines are for DF calculations. Dotted line indicates the calculation with the original Paris zero-range exchange term; thin solid line, calculation with  $G_{E\delta m} = -752 \text{ MeV fm}^3$  ( $\Delta G_{E\delta} = -160 \text{ MeV fm}^3$ ); thick solid line with dots,  $G_{E\delta m} = -942 \text{ MeV fm}^3$  ( $\Delta G_{E\delta} = -350 \text{ MeV fm}^3$ ).

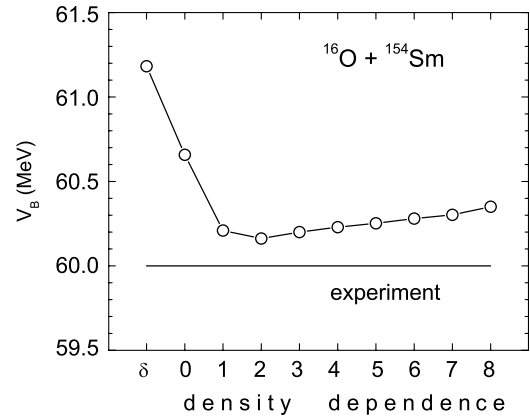


FIG. 5. Calculated fusion barrier energies for the reaction  $^{16}\text{O} + ^{154}\text{Sm}$  (target nucleus is considered spherical) for all types of DF calculation, namely zero-range ( $\delta$ ) and finite-range density independent (0) and density-dependent (1–8) interactions. Experimentally determined average barrier energy is indicated by the horizontal line.

determined average barrier energy is indicated by the horizontal line. The DD2 version of the density-dependent  $NN$  interaction provides the minimum value of the barrier energy, which is the closest to the experimental value. Therefore, we made an additional modification to the strength of the zero-range exchange interaction with the aim to reproduce this minimum value of  $V_B$ . The value of  $\Delta G_{E\delta} = -350 \text{ MeV fm}^3$  was found to be suitable for this purpose in the case under consideration. The barrier distribution calculated with the modified  $G_{E\delta m} = -942 \text{ MeV fm}^3$  is presented in Fig. 4 by the solid line with dots. These calculations agree with the data quite well.

#### B. Other reactions with statically deformed nuclei

The results of calculations for the other six reactions listed in Table I are presented here, using the same modification of the Paris zero-range exchange interaction as above. Comparisons with experimental barrier distributions for these reactions are made in Figs. 6 and 7. The average barrier energies of the experimental distributions are reproduced quite well by these calculations, which also almost matched the  $^{16}\text{O} + ^{154}\text{Sm}$  data. At the lower energies, the calculations generally agree well with the data. However, in most cases, the higher energy peak associated with collisions with the equator of the prolate deformed target nuclei has a significantly larger weight in the calculations.

This could have three distinct causes: (i) the deformation parameters are not correct, (ii) the DFM input parameters are not correct, or (iii) other physics is not included in the model.

For the target nuclei  $^{154}\text{Sm}$ ,  $^{232}\text{Th}$ , and  $^{238}\text{U}$ , the deformation and DFM input parameters were taken from the self-consistent electron scattering analysis of Ref. [24]. Thus, the degree of agreement between the calculated and measured  $D(E_{c.m.})$  in Figs. 4, 6, and 7 may reflect the degree of overlap between the physics of electron scattering and the more complex situation of heavy-ion interactions.

The parameters for the other deformed nuclei are less well defined. For  $^{186}\text{W}$  [see Fig. 6(a)], the only parameters of

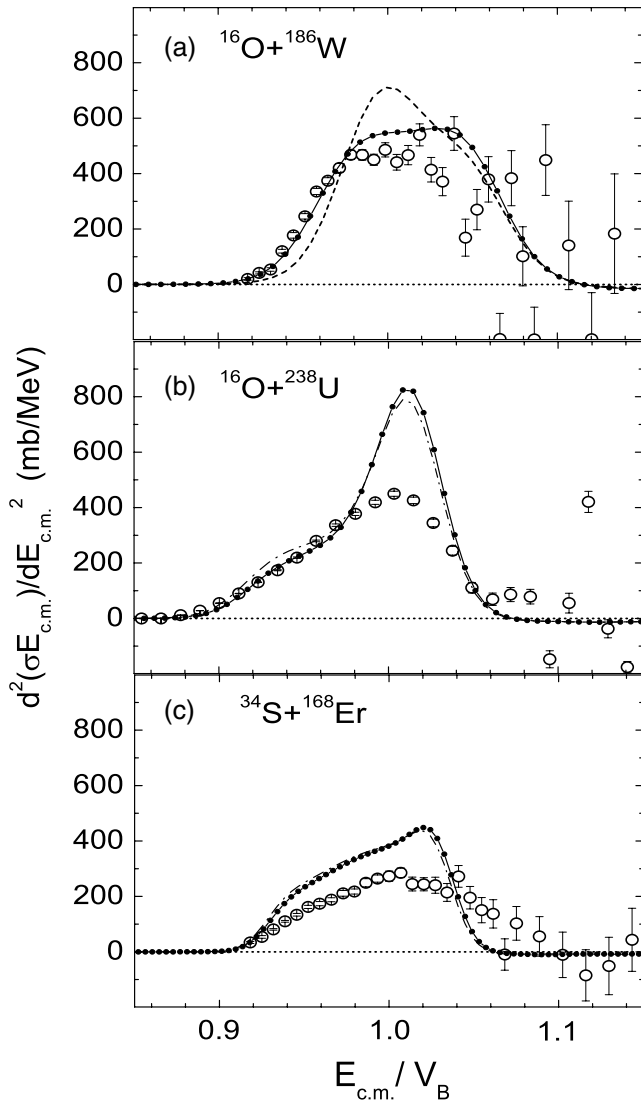


FIG. 6. Barrier distributions calculated using the DFM (thick solid lines with dots) with the zero-range modified exchange term ( $\Delta G_{E\delta} = -350 \text{ MeV fm}^3$ ) are compared with the experimental data (open circles) from Refs. [4] ( $^{16}\text{O} + ^{186}\text{W}$ ), [6] ( $^{16}\text{O} + ^{238}\text{U}$ ), and [5] ( $^{34}\text{S} + ^{168}\text{Er}$ ). Dashed line in (a) represents the DF calculations with theoretical values for deformation parameters  $\beta_{2,4,6} = 0.230, -0.107, 0$  from Ref. [32]. Dash-dotted lines in (b) and (c) represent the  $D(E_{\text{c.m.}})$  obtained using the angular-dependent matter diffuseness for the target nuclei. Here and in the figures below  $V_B$  denotes the spherical barrier energy calculated with the modified Paris zero range exchange interaction.

the density distribution which we are aware of come from Ref. [26]. However, in that work the electron scattering data were analyzed under the assumption that the target nuclei density distribution did not possess any deformation, i.e., a spherically symmetric 2pF distribution was used. It is intrinsically inconsistent to use the values of  $R_T$  and  $a_T$  obtained in this way, while simultaneously treating  $^{186}\text{W}$  as a deformed nucleus. Moreover, no experimental information about the values of  $\beta_4$  and  $\beta_6$  are known to us. The value of  $\beta_2 = 0.2238$  tabulated in Ref. [31] is very close to the

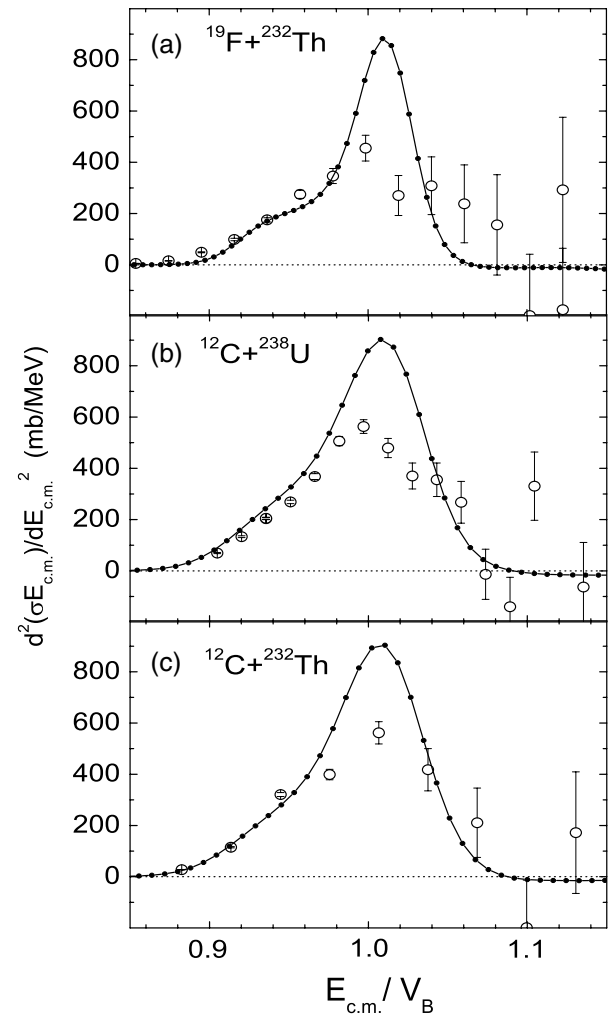


FIG. 7. Same as in Fig. 6. Experimental data are from Refs. [27] ( $^{19}\text{F} + ^{232}\text{Th}$  and  $^{12}\text{C} + ^{238}\text{U}$ ) and [7] ( $^{12}\text{C} + ^{232}\text{Th}$ ).

theoretically predicted 0.230 from Ref. [32]. The values of  $\beta_4 = -0.107$  and  $\beta_6 = 0$  have been predicted in that work. Thus, we used those theoretical values for all deformation parameters in the calculations presented in Fig. 6(a) by the dashed line. The agreement with the data is much worse than for  $^{154}\text{Sm}$ . Since no consistent input parameter set is available for  $^{186}\text{W}$ , we feel free to vary the deformation parameters. The calculation shown in Fig. 6(a) by the thick solid line with dots was performed with  $\beta_{2,4,6} = 0.31, -0.030, 0$  according to Ref. [4]. It agrees quite well with the data; even the height of the peak of  $D(E_{\text{c.m.}})$  is reproduced. For the reaction of Fig. 6(c),  $^{34}\text{S} + ^{168}\text{Er}$ , the values of the input parameters are also not well defined. The values of  $R_T$  and  $a_T$  are not available in the literature. Therefore, we used the values of these parameters as presented in Ref. [25] for  $^{166}\text{Er}$ . However, the values in Ref. [25] came from Ref. [24], which stressed that it was not possible to fit satisfactorily the electron scattering data with the 2pF profile of Eq. (18). For the deformation parameters, we took the values  $\beta_{2,4,6} = 0.338, 0.0, 0.025$  according to Ref. [5]. In this set, the value of the hexacontatetrapole deformation has the opposite sign to that theoretically predicted in Ref. [32].

Turning to the DFM input parameters, it is important to note that up to now all our calculations have been performed with a constant (angular-independent) matter diffuseness. In order to demonstrate the effect of the (theoretically required) angular dependence discussed previously, we performed such calculations for the reactions of Figs. 6(b) and 6(c),  $^{16}\text{O} + ^{238}\text{U}$  and  $^{34}\text{S} + ^{168}\text{Er}$ . The resulting  $D(E_{c.m.})$  are presented there by dashed-dotted lines. Comparing these with the  $D(E_{c.m.})$  calculated using the constant  $a_T$ , we conclude that the angular dependence, although not of crucial importance, is significant in the case of the  $^{16}\text{O} + ^{238}\text{U}$  reaction for the low-energy shoulder (the experimental errors in this region are much smaller than the symbol size). Thus, it would be interesting to reanalyze the data on electron elastic scattering using an angular-dependent diffuseness of the matter distribution.

It is noticeable in Figs. 6 and 7 that for the reactions with uranium and thorium target nuclei, the calculated  $D(E_{c.m.})$  are much too high at their maxima in comparison with the data. At the same time, for the  $^{16}\text{O} + ^{154}\text{Sm}$  reaction (see Fig. 4), the agreement between calculated and measured  $D(E_{c.m.})$  is much better. Since the shape of the  $D(E_{c.m.})$  is believed to be dominated by the deformation of these target nuclei, one might have expected a similar degree of agreement or disagreement for these reactions involving  $^{154}\text{Sm}$ ,  $^{232}\text{Th}$ , and  $^{238}\text{U}$  (see Table I). Let us focus on the barrier distributions for the reactions  $^{16}\text{O} + ^{154}\text{Sm}$  (Fig. 4) and  $^{16}\text{O} + ^{238}\text{U}$  [Fig. 6(b)]. The ratio of the calculated  $D(E_{c.m.})$  at the peak  $D_{pDF}$  to the experimental one  $D_{pexp}$  is equal to 1.2 in Fig. 4; whereas for the second reaction,  $D_{pDF}/D_{pexp}$  is as large as 1.9. The reason for that is the following. The values of the  $D_{pexp}$  are approximately 600 mb/MeV for the samarium target nucleus and only 450 mb/MeV for the uranium. From the values of the quadrupole deformation, which are 0.311 for the former case and 0.261 for the latter case, the opposite is expected: the larger the value of  $\beta_2$ , the flatter the barrier distribution.

Another source of difference between these two reactions is the matter diffuseness, which is different for  $^{154}\text{Sm}$  and  $^{238}\text{U}$  by some 15% as seen in Table I. Thus, in Fig. 8 we present the  $D(E_{c.m.})$  calculated for the  $^{16}\text{O} + ^{238}\text{U}$  reaction

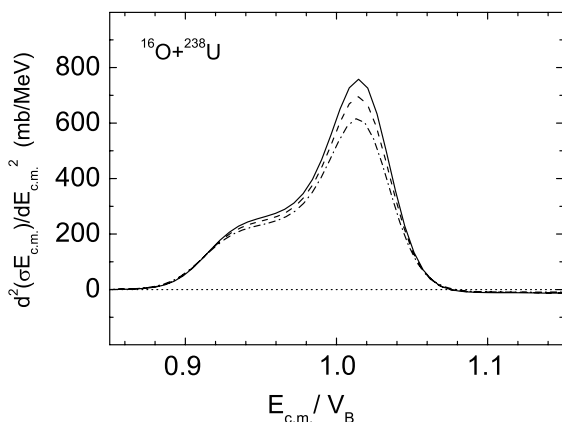


FIG. 8. Barrier distributions calculated using the DFM for the  $^{16}\text{O} + ^{238}\text{U}$  reaction with three values of  $a_T$ : 0.596 fm (solid line), 0.479 fm (dashed line), and 0.343 fm (dashed-dotted line). Deformation parameters are  $\beta_{2,4,6} = 0.311, 0.087, -0.018$ .

with  $\beta_{2,4,6} = 0.311, 0.087, -0.018$  (which are standard for samarium), but with different values of the diffuseness  $a_T$ : 0.569 fm, the standard value for uranium (solid line); 0.479 fm, the standard value for samarium (dashed line); and 0.343 fm for illustrative purposes (dashed-dotted line). It is clearly seen from this figure that the value of  $D_{pDF}$  decreased down to 700 mb/MeV in the case of  $a_T = 0.479$  fm, which is still much higher than the experimental value of 450 mb/MeV seen in Fig. 6 for  $^{238}\text{U}$ . The area under the barrier also decreases as the diffuseness is reduced. This can be explained by the smaller barrier radius (and thus higher barrier) that results with a smaller matter diffuseness. Thus, reasonable variation of the matter diffuseness cannot alone explain the difference between measurements and calculations for the  $^{16}\text{O} + ^{238}\text{U}$  reaction as well as the difference between the  $D(E_{c.m.})$  for the  $^{16}\text{O} + ^{238}\text{U}$  and  $^{16}\text{O} + ^{154}\text{Sm}$  reactions.

One more possible source of the difference is purely a size effect. In order to explore it, we calculated  $D(E_{c.m.})$  for four reactions involving  $^{238}\text{U}$ ,  $^{208}\text{Pb}$ ,  $^{154}\text{Sm}$ , and  $^{90}\text{Zr}$  as the target nuclei. For this comparison, we used in all cases the same projectile nucleus  $^{16}\text{O}$ , the same values of the deformation parameters  $\beta_{2,4,6} = 0.311, 0.087, -0.018$ , and the same value of  $a_T = 0.479$  fm. The values of  $R_T$  were of course different: for  $^{238}\text{U}$  and  $^{154}\text{Sm}$ , they are presented in Table I; for  $^{208}\text{Pb}$  and  $^{90}\text{Zr}$ , the values of 6.631 and 4.878 fm were taken (see Table VII of Ref. [10]). The classical, sharply defined barrier distribution is smoothed by quantum-tunneling through the barrier. The energy smoothing width due to tunneling is expected to be similar for each reaction, but the absolute width of the barrier distribution should scale with  $Z_T$ , thus relatively more smoothing should occur for the lighter nucleus. To illustrate this, the calculations were normalized by dividing by the average barrier energy and are shown in Fig. 9(a), where it is clear that as expected, the smoothing of the barrier distribution evolves monotonically on this scale, becoming larger as  $a_T$  decreases. This is why the structure disappears as the target nucleus becomes lighter. Thus, the systems with a higher average fusion barrier should give a better “resolution” for the structure of the barrier distribution, since the relative contribution of the smoothing due to quantum tunneling is reduced. The experimental barrier distributions for the  $^{16}\text{O} + ^{238}\text{U}$  and  $^{16}\text{O} + ^{154}\text{Sm}$  reactions, normalized as above, are shown in Fig. 9(b). In contrast with the theoretical calculations above, the data for the two reactions show almost no difference in the shapes of the barrier distributions. Thus, the different level of agreement between data and calculations for the  $^{16}\text{O} + ^{238}\text{U}$  and  $^{16}\text{O} + ^{154}\text{Sm}$  reactions appears to result to a large extent from differences in the calculations, rather than differences in the measurements. This difference may well be due to couplings to vibrational states (which on average will scale with the barrier energy) and transfer channels, which are not within the scope of the present geometrical calculations.

The deformations of samarium and uranium target nuclei are only slightly different (see Table I). In order to see the impact on  $D_{pDF}$  of changes in deformation, we present in Fig. 10 the barrier distributions calculated for the reaction  $^{16}\text{O} + ^{238}\text{U}$  with several sets of different target nucleus deformations. The solid curve with dots represents the basic set of

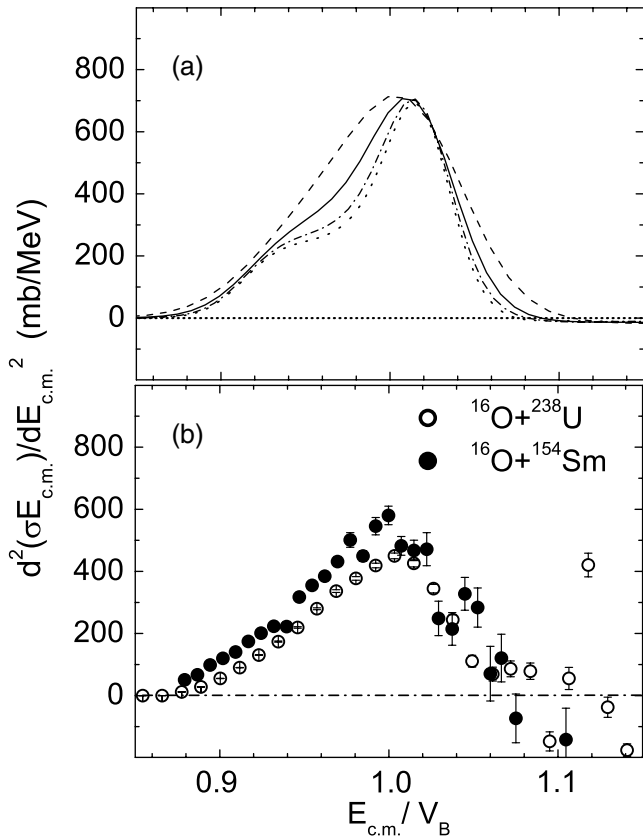


FIG. 9. (a) Barrier distributions calculated using the DFM for four reactions with the same  $a_T = 0.48$  fm,  $\beta_{2,4,6} = 0.311, 0.87, -0.018$ , and  $^{16}\text{O}$  as projectile nucleus. Target nuclei are  $^{90}\text{Zr}$  (long dashed line),  $^{154}\text{Sm}$  (solid line),  $^{208}\text{Pb}$  (dashed-dotted line), and  $^{238}\text{U}$  (short dashed line). (b) Experimental barrier distributions for two reactions. For each reaction, the collision energy in the center-of-mass frame was divided by its barrier energy.

$\beta_{2,4,6} = 0.261, 0.087, 0$ . The thin solid curve was obtained with the deformation parameters of  $^{154}\text{Sm}$ :  $\beta_{2,4,6} = 0.311, 0.087, -0.018$ . The increase of the quadrupole deformation brings the peak value of  $D_{p\text{DF}}$  down significantly. The small hexacontatetrapole deformation is insignificant for the peak value of the barrier distribution, as seen from the dashed line obtained with  $\beta_{2,4,6} = 0.311, 0.087, 0$  (but it is significant for the low-energy part of  $D(E_{c.m.})$  as seen in the figure). The next calculation was performed without hexadecapole deformation and with the original value of the quadrupole deformation of uranium ( $\beta_{2,4,6} = 0.261, 0, 0$ , thick solid line without dots). The absence of  $\beta_4$  appears to be very important for the peak value of the barrier distribution which decreases by 30%. Finally, we show by the dashed-dotted line the  $D(E_{c.m.})$  calculated with extremely large value of  $\beta_2 = 0.338$ , which is inherent to  $^{168}\text{Er}$ . In this case, the  $D_{p\text{DF}}$  decreases down to the value of 600 mb/MeV but the shape of  $D(E_{c.m.})$  is significantly different from the experimental one.

To summarize, it seems impossible to explain in detail the experimental results within the framework of this DFM approach. The experimental data themselves in Refs. [4–7] were obtained by including proper exit channels. For instance,

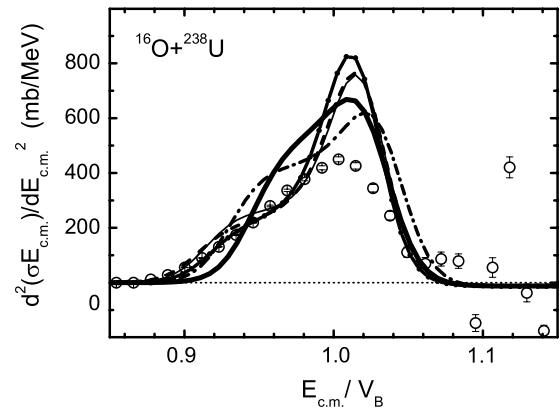


FIG. 10. Barrier distributions for the  $^{16}\text{O} + ^{238}\text{U}$  reaction. Open circles show the experimental data of Ref. [6]; lines represent results of the DFM calculations. Thick solid line with dots is for  $\beta_{2,4,6} = 0.261, 0.87, 0$ ; thin solid line,  $\beta_{2,4,6} = 0.311, 0.87, -0.018$ ; dashed line,  $\beta_{2,4,6} = 0.311, 0.87, 0$ ; thick solid line without symbols,  $\beta_{2,4,6} = 0.261, 0, 0$ ; and dashed-dotted line,  $\beta_{2,4,6} = 0.338, 0, 0$ .

in the case of the samarium target nucleus, the evaporation residue formation represents the fusion cross section whereas the fission probability is negligible. In the case of the uranium target nucleus, the situation is opposite: the probability of compound nucleus survival after emitting several neutrons is totally negligible in comparison with the fusion-fission process. Since no reasonable variation of the input parameters of the DFM results in detail agreement with the data, physical effects not included in this approach should then be responsible. One of these may be the effect of ignoring the different geometry involved in tangential motion, which is not accounted for when absorbing that motion into a centrifugal potential. Another may be coupling to vibrational states in the deformed target nucleus, which will certainly reduce the height of the peak. A third effect may arise from processes (such as deep-inelastic scattering) competing with fusion, as discussed in Ref. [33], although conventional expectations based on the light projectiles and low energies would not favor this explanation. It may be that these competing processes depend on the orientation of the deformed nucleus, adding another layer of complexity to the situation.

The second objective of this work—to compare the DFM calculation of barrier distributions with a simpler geometrical approach—can be achieved independently of these experimental complications and is carried out below.

### C. Approximating the double-folding potential by a Woods-Saxon potential: Importance of finite size corrections

As already discussed in the introduction, the analysis of experimental  $D(E_{c.m.})$  was performed in many papers using the center-line WS potential of Eq. (2) in which finite size effects are implicitly ignored. An approximate study of these effects performed in Ref. [9] showed their significant impact on the near-barrier fusion cross sections and on the shapes of the corresponding  $D(E_{c.m.})$ .

TABLE II. DFM barrier radii  $R_B$  and energies  $V_B$ , depths  $V_{WS}$ , radius parameters  $r_{WS}$ , and diffusenesses  $a_{WS}$  of the WSP that is the best approximation to the DFM potential. Calculations were performed assuming spherical target nuclei; in the DFM calculations, the value  $G_{E\delta m} = -942 \text{ MeV fm}^3$  was used. In the last column, the deviation of the WSP from the DFM potential is indicated (see text).

Reaction	$R_B$ (fm)	$V_B$ (MeV)	$V_{WS}$ (MeV)	$r_{WS}$ (fm)	$a_{WS}$ (fm)	$\chi_R^2$ ( $10^{-4}$ )
$^{16}\text{O} + ^{154}\text{Sm}$	11.19	60.13	1380	0.93	0.65	1.1
$^{16}\text{O} + ^{186}\text{W}$	11.81	69.40	1240	0.97	0.63	1.3
$^{16}\text{O} + ^{238}\text{U}$	12.19	81.94	1160	0.96	0.70	0.7
$^{34}\text{S} + ^{168}\text{Er}$	12.10	122.00	1440	0.96	0.70	0.7
$^{19}\text{F} + ^{232}\text{Th}$	12.27	89.53	1320	0.95	0.71	0.7
$^{12}\text{C} + ^{238}\text{U}$	12.08	62.02	1160	0.95	0.70	0.8
$^{12}\text{C} + ^{232}\text{Th}$	11.96	61.37	1300	0.95	0.67	1.0

Since all the finite size effects are included automatically in the DFM calculations, we can now investigate this question in a more rigorous way. To that end, we fitted a Woods-Saxon potential to the DF potential in the region of the fusion barrier. This was done for each reaction considering the target nucleus as a spherical one with the parameters  $R_T$  and  $a_T$  from Table I. In order to estimate the quality of the fit, we calculated a relative error

$$\chi_R^2 = \frac{1}{N} \sum_{i=1}^N \left( \frac{U_{DF}(R_i) - U_{WS}(R_i)}{U_{DF}(R_i) + U_{WS}(R_i)} \right)^2 \quad (20)$$

for distances  $R_i$  around the fusion barrier radius  $R_B$ , over the range  $R_B - 1 < R_i < R_B + 1 \text{ fm}$ . The parameters of the WSP were allowed to vary within the following ranges, with steps as shown:  $1500 < V_{WS} < 1000 \text{ MeV}$ ,  $\Delta V_{WS} = 20 \text{ MeV}$ ;  $1.2 < r_{WS} < 0.8 \text{ fm}$ ,  $\Delta r_{WS} = 0.01 \text{ fm}$ ;  $0.5 < a_{WS} < 1.2 \text{ fm}$ ,  $\Delta a_{WS} = 0.01 \text{ fm}$ . The parameters of the WS potentials providing the best fits to the DF potentials are presented in Table II along with the values of  $\chi_R^2$ .

The quality of the fit depends mainly upon the value of the diffuseness  $a_{WS}$ . It is found to be around 0.6–0.7 fm, a

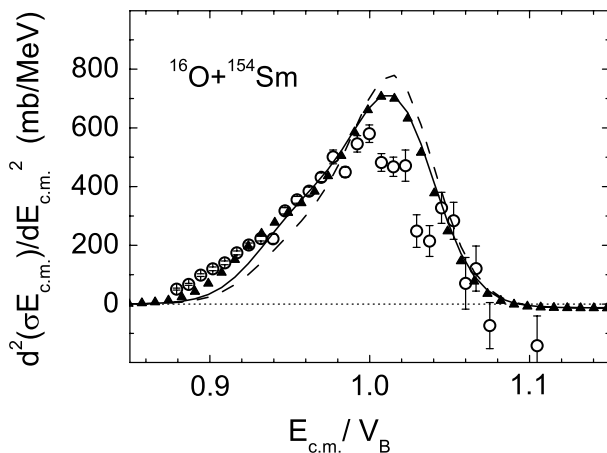


FIG. 11. Barrier distributions for the  $^{16}\text{O} + ^{154}\text{Sm}$  reaction. Open circles show the experimental data of Ref. [4]; solid triangles, DF calculations; dashed line, WSCL calculation; solid line, calculation using the WSSC potential.

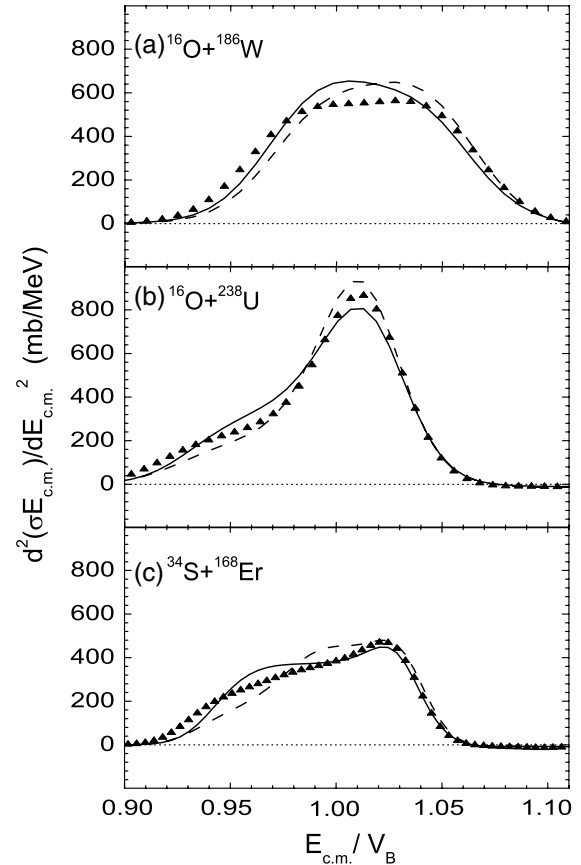


FIG. 12. Barrier distributions calculated for three reactions in Fig. 6. Solid triangles are for DF calculations; thick dashed lines, WSCL calculations; thick solid lines, calculations using the WSSC potential.

value significantly lower than the  $\approx 1 \text{ fm}$  required by the experimental data (see a survey of the experimental diffusenesses in Ref. [33]). The question of the equivalent diffusenesses of the DF potential was discussed in detail in Ref. [10], which showed that the WS potential with  $a_{WS} \approx 1 \text{ fm}$  provided a very poor approximation of the DF potential. The depth  $V_{WS}$  and the radius parameter  $r_{WS}$  of the WS show correlation and influence the value of  $\chi_R^2$  rather weakly.

Now in Fig. 11, we compare the  $D(E_{c.m.})$  calculated using the DF potential (triangles), the center-line Woods-Saxon potential without curvature corrections (WSCL, dashed line), and the minimum distance Woods-Saxon potential corrected for the curvature of the target nucleus (WSSC, solid line). These calculations were performed for the  $^{16}\text{O} + ^{154}\text{Sm}$  reaction. It is clearly seen in this figure that accounting for the finite size corrections definitely improves the quality with which the WS potential reproduces the  $D(E_{c.m.})$  obtained using the DF potential. In particular, in the WSSC calculations, in comparison with the WSCL calculations, the height of the peak moves down and the low-energy shoulder shifts up closer to the  $D(E_{c.m.})$  obtained using the DFM and to the experimental points (open circles).

In Figs. 12 and 13, the same comparison between three types of calculations (using the DFP, WSCL, and WSSC) for

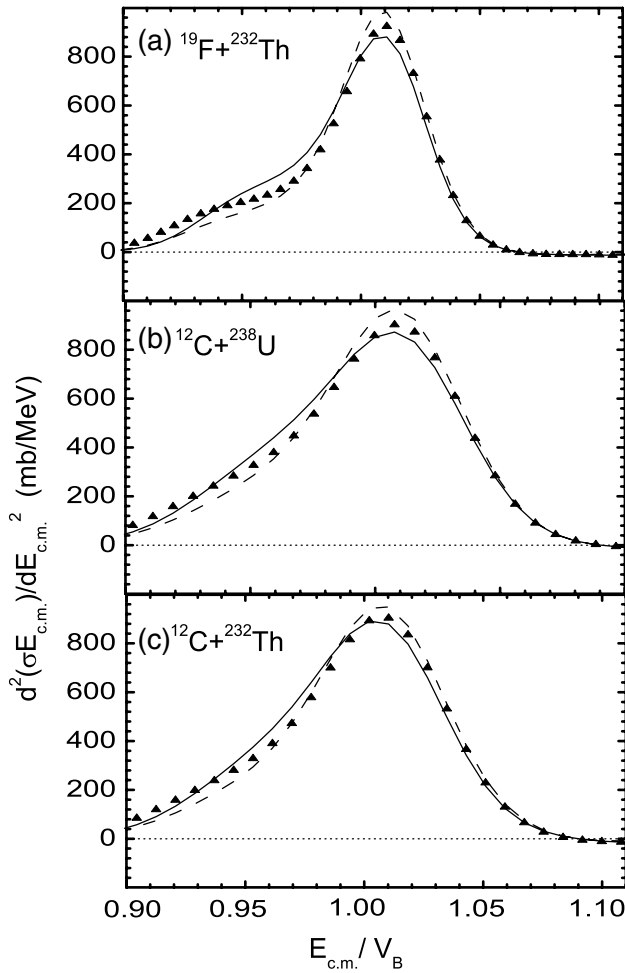


FIG. 13. Same as Fig. 12, but for reactions in Fig. 7.

the other six reactions under consideration is presented. The notations for the barrier distributions are as in Fig. 11 except for clarity we do not show the experimental data points. For all six reactions, accounting for the finite size effects in the WS potential elevates the lower energy ( $E_{c.m.}/V_B \leq 0.97$ ) shoulder of the  $D(E_{c.m.})$ , thereby in general improving agreement with the DF calculations. Quantitatively, however, both the WSCL and the WSSC calculations deviate from the DF results by much more than 10%, which is a typical experimental error of the  $D(E_{c.m.})$  in the region  $E_{c.m.}/V_B \leq 0.97$ .

It would be too optimistic, however, to expect the barrier distributions calculated using the WSSC to coincide perfectly with those using the DFP. At the moment, we see two reasons for that. First, the WSSC treats the finite size effects only approximately whereas the DFP does that exactly. The second and clearer point is that we fit a WSP to the DFP calculated assuming a spherical target nucleus. Certainly, the barrier energies obtained for a deformed target nucleus with this fitted WSP can deviate from the corresponding values of  $V_B(\theta)$  obtained using the DFM. This consideration is quantified in Figs. 14 and 15 for the  $^{16}\text{O} + ^{154}\text{Sm}$  and  $^{19}\text{F} + ^{232}\text{Th}$  reactions, respectively. The barrier energies plotted in the upper panels of these figures have been calculated for zero angular momentum

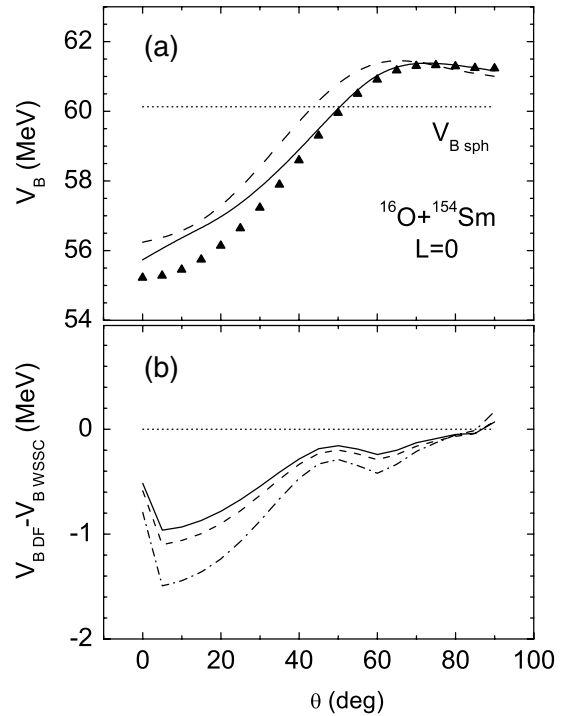


FIG. 14. Results of the DFM and WS calculations for the reaction  $^{16}\text{O} + ^{154}\text{Sm}$ . (a) Barrier energies calculated for zero angular momentum using the DFM (triangles), WSCL (dashed line), WSSC (solid line). (b) Differences  $V_{BDF} - V_{BWSSC}$  are presented for  $L = 0$  (solid lines),  $L = 20$  (dashed lines), and  $L = 40$  (dashed-dotted lines).

using the DFM (solid triangles), center-line Woods-Saxon potential (dashed lines), and WSSC (solid lines). Substantial

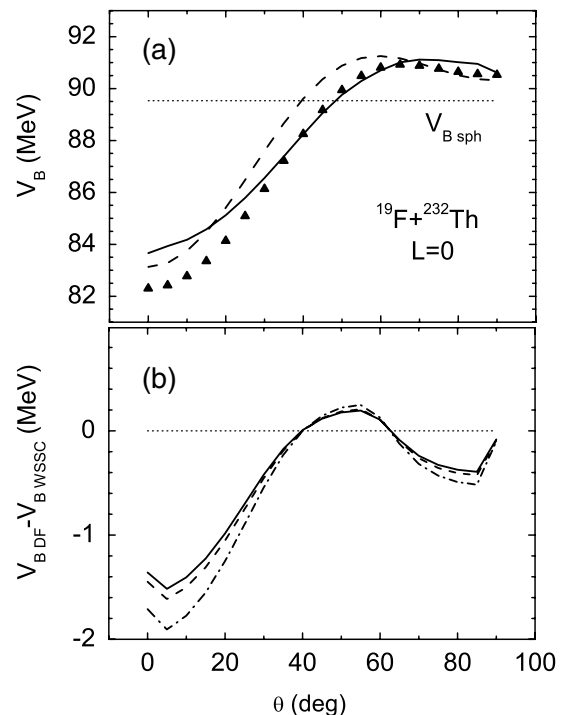


FIG. 15. Same as Fig. 14, but for  $^{19}\text{F} + ^{232}\text{Th}$ .

TABLE III. As in Table II, except the WSP was fitted to the DFP at each individual angle  $\theta$  for  $^{16}\text{O} + ^{154}\text{Sm}$ .

$\theta$ (deg)	$R_B$ (fm)	$V_B$ (MeV)	$V_{WS}$ (MeV)	$r_{WS}$ (fm)	$a_{WS}$ (fm)	$\chi_R^2$ ( $10^{-5}$ )
0	12.68	55.22	1020	0.98	0.64	5.1
10	12.60	55.45	1180	0.97	0.64	1.8
20	12.38	56.14	1440	0.95	0.65	2.0
30	12.05	57.23	1080	0.98	0.64	4.3
40	11.65	58.59	1140	0.97	0.65	2.0
50	11.26	59.95	1380	0.95	0.65	6.0
60	10.98	60.91	1420	0.94	0.65	5.3
70	10.81	61.30	1400	0.94	0.64	5.1
80	10.77	61.29	1020	0.96	0.64	5.2
90	10.77	61.23	1120	0.95	0.64	4.8

deviations (up to  $\approx 1$  MeV) of the  $V_{BWS}$  from the  $V_{BDF}$  are clearly seen. The discrepancy between the  $V_{BWS}$  and the  $V_{BDF}$  increases with  $L$  as the lower panels of Figs. 14 and 15 demonstrate. Here the differences  $V_{BDF} - V_{BWS}$  are presented for  $L = 0$  (solid lines),  $L = 20$  (dashed lines), and  $L = 40$  (dashed-dotted lines). Obviously the use of the WSP fitted to the DFP for the spherical target nucleus is a significant (and inevitable) source of the quantitative difference between the  $D(E_{c.m.})$  calculated using the double-folding model and the Woods-Saxon potential including the finite size corrections.

This does not mean that the DFP cannot be approximated by a WSP in the case of a deformed target nucleus. But the parameters of the WSP providing the best fit for the DFP for a deformed target nucleus should be angle dependent and deviate from those fitted to the spherical case. We performed such a fit at several values of  $\theta$  for the  $^{16}\text{O} + ^{154}\text{Sm}$  reaction with the deformed target and found the results presented in Table III. The quality of the fit is very good.

Concluding this section, we have to conclude that the DFP cannot be substituted by a center-line WS potential without curvature corrections, WSCL, for calculating the  $D(E_{c.m.})$  for reactions with deformed target nuclei. Even the minimum distance Woods-Saxon potential corrected for the curvature of the target nucleus, WSSC, does not result in  $D(E_{c.m.})$  which agree (within typical accuracy of the experimental data) with those calculated using the DF potential. This proves the significance of carrying out an accurate treatment of finite size effects in modeling the fusion process at near-barrier energies.

#### IV. CONCLUSIONS

This study was devoted to two questions. First, we wanted to see to what extent the double-folding model could describe the measured fusion barrier distributions for reactions involving deformed target nuclei. The second objective was to check the effect of the finite size of the deformed target nucleus by means of comparison between the fusion barrier distributions calculated using the DFM and the center-line Woods-Saxon potentials.

To find the answers to these questions, we developed a new computer code that allowed the calculation, using the DFM

with M3Y effective  $NN$  interactions, of the fusion barriers, cross sections, and resulting barrier distributions for reactions involving deformed target nuclei (quadrupole, hexadecapole, and hexacontatetrapole deformations were accounted for).

This study showed that the angular dependence of the fusion barriers calculated with a zero-range exchange term for the  $NN$  interaction is very similar to that obtained using a finite-range interaction. Thus, the rather time-consuming finite-range calculations are successfully avoided by applying an appropriately modified zero-range exchange term. Moreover, a modification was found that mimicked the density dependence of the M3Y effective  $NN$  interaction.

This code was applied to seven heavy-ion fusion reactions involving deformed target nuclei. The fusion barrier distributions were found generally only to give qualitative agreement with the measurements, being somewhat sharper peaked. A range of physical effects were suggested that may need to be incorporated into calculations before heavy-ion fusion barrier distributions can give information on static deformation.

As existing interpretations of experimental  $D(E_{c.m.})$  have been usually carried out using a Woods-Saxon shape for the nuclear part of the nucleus-nucleus potential, we fitted the spherical double-folding potentials at the barrier radii by a Woods-Saxon form. The  $D(E_{c.m.})$  calculated with this fitted WS potential, but now accounting for the deformation of the target nuclei, are significantly different from the  $D(E_{c.m.})$  calculated using the double-folding potential. This indicates that the finite size effects are substantial and should be accurately incorporated into any meaningful analysis of experimental fusion cross sections and barrier distributions for reactions involving statically deformed nuclei.

#### ACKNOWLEDGMENT

M.D. and D.J.H. acknowledge the support of an ARC Discovery Grant.

#### APPENDIX A: ANGULAR MOMENTUM DEPENDENCE

The approaches to treating the angular momentum dependence of the fusion barrier parameters taken here, and in Refs. [11,29] are compared and discussed. In those papers, fusion cross sections were calculated for the  $^{16}\text{O} + ^{154}\text{Sm}$  reaction by performing the summation over  $L$  in Eq. (16) analytically, thus reducing significantly the computer time used. To do that, the following approximations were used in Ref. [11]:

$$\omega_B(L, \theta) \approx \omega_B(0, \theta), \quad (\text{A1})$$

$$V_B(L, \theta) \approx V_B(0, \theta) - \frac{\hbar^2 L(L+1)}{2\mu R_B(0, \theta)}. \quad (\text{A2})$$

In Ref. [29],  $\hbar\omega_B(L, \theta) = 7.3$  MeV and Eq. (A2) was used. We show here the effect of making those approximations and explain why instead we calculate numerically all barrier radii  $R_B(L, \theta)$ , energies  $V_B(L, \theta)$ , and frequencies  $\omega_B(L, \theta)$ .

In Fig. 16, we show the barrier distributions calculated using the DFM with three constant (i.e.,  $L$  and  $\theta$  independent) values of the barrier frequency, namely,  $\hbar\omega_B = 4, 6,$  and  $8$  MeV,

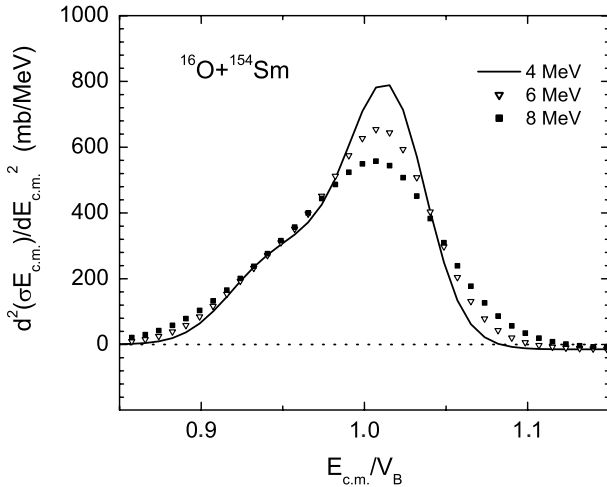


FIG. 16. Barrier distributions calculated using the DFM with constant ( $L$  and  $\theta$  independent) values of the barrier frequency  $\omega_B$ . Values of  $\hbar\omega_B$  are indicated in the figure.

representing the typical range of values for different  $L$  and  $\theta$ . Qualitatively, the  $D(E_{c.m.})$  remains the same as the value of the frequency changes. However, the finite size effects we are aiming to investigate are of order of 20%, as shown in

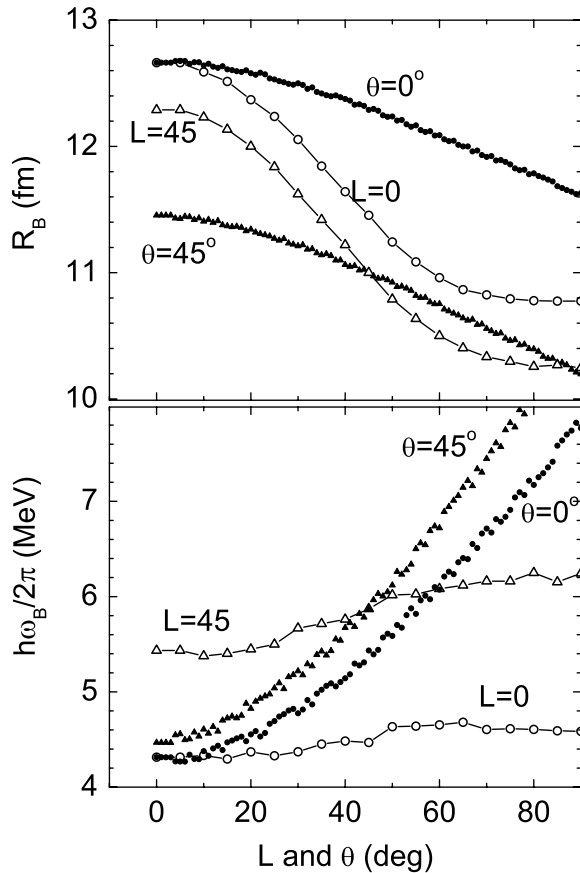


FIG. 17. Barrier radii  $R_B$  (upper panel) and the barrier frequencies  $\hbar\omega_B$  (lower panel) vs the angular momentum  $L$  (solid symbols) and  $\theta$  (open symbols connected by lines). Calculations were performed for  $^{16}\text{O} + ^{154}\text{Sm}$  using the DFM.

Fig. 4 of Ref. [9]. The quantitative difference of the barrier distributions calculated with the different values of  $\hbar\omega_B$  is certainly significant on this scale. Thus, the approximation of a constant frequency should be avoided.

To see to what extent it is convenient for us to use  $L$ -independent  $R_B(\theta)$  and  $\omega_B(\theta)$ , let us inspect Fig. 17. Here the horizontal axis is used simultaneously for  $L$  and  $\theta$ . The  $L$ -dependent barrier radii  $R_B(L)$  and barrier frequencies  $\hbar\omega_B(L)$  are shown by solid symbols, whereas the  $\theta$ -dependencies of these quantities are presented by open symbols. The  $L$  dependencies were calculated at  $\theta = 0^\circ$  and  $45^\circ$ . The  $\theta$  dependencies were calculated at  $L = 0$  and  $L = 45$ . These calculations were performed for the  $^{16}\text{O} + ^{154}\text{Sm}$  reaction using the DFM.

The upper panel of Fig. 17 shows that the  $L$  dependence of the barrier radii is indeed significantly weaker than their  $\theta$  dependence. However, the situation is certainly opposite for the barrier frequencies: they change faster with  $L$  than with  $\theta$ . Thus, if one does not neglect the  $\theta$  dependence of the frequency, it is intrinsically inconsistent to neglect its  $L$  dependence.

#### APPENDIX B: COMPARISON WITH PREVIOUS DFM CALCULATIONS

To check the consistency of our computer code with a previous deformed DFM code, we made calculations for the  $^{16}\text{O} + ^{154}\text{Sm}$  reaction, taking the same input parameters as in Ref. [11]. In Table I of that work, the values of the ratio  $U_{nE\delta}/U_{nEf}$  were presented. We compare the values calculated using our code to those of Ref. [11] in Fig. 18. The target deformation (if applied) was taken to be purely quadrupole with  $\beta_2 = 0.36$ . The lines represent our results whereas the large solid symbols show the values presented in Ref. [11].

The trend of the results can be easily understood in the following qualitative way. The finite-range exchange part

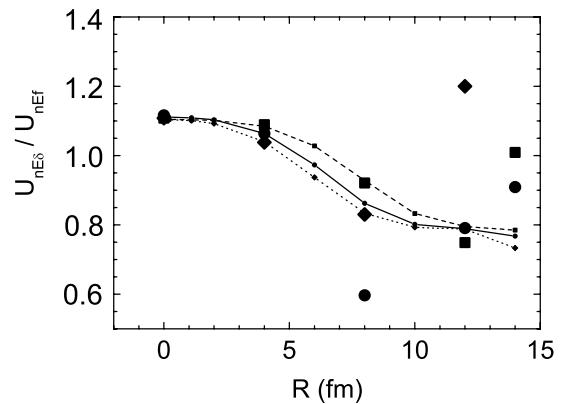


FIG. 18. The zero-range exchange nucleus-nucleus interaction,  $U_{nE\delta}$ , divided by the finite-range interaction,  $U_{nEf}$ , for the Paris interaction calculated for  $^{16}\text{O} + ^{154}\text{Sm}$ . Lines correspond to the present calculations; symbols are from Table 1 of Ref. [11]. Solid line and circles are for the spherical target nucleus. Other calculations were performed for the deformed target with  $\beta_{2,4,6} = 0.36, 0, 0$ . Dashed line and squares are for  $\theta = 0^\circ$ ; dotted line and diamonds,  $\theta = 90^\circ$ .

of the Paris  $NN$  interaction is attractive for any distances (see Table I of Ref. [10] or Eq. (19b) of Ref. [11]). The zero-range exchange interaction appears to be only due to the density overlap of the colliding nuclei, whereas the finite-range interaction is due to both the density overlap and the finite radius of the interaction itself. The larger the distance between the centers of mass, the smaller is the density overlap. Thus, for any value of  $\theta$ , the ratio  $U_{nE\delta}/U_{nEf}$  should decrease as  $R$  becomes larger. Moreover, it is not the center-of-mass distance that controls the strength of the nuclear interaction, but rather the surface-to-surface distance  $S$ . For a fixed value of  $R$ ,  $S$  takes (for the chosen deformation) the largest value for  $\theta = 90^\circ$  and becomes the smallest at  $\theta = 0^\circ$ . In the case of a spherical target,  $S$  is expected to take an intermediate value. Thus, the ratio  $U_{nE\delta}/U_{nEf}$  is expected to take the smallest value at  $\theta = 90^\circ$  and the largest at  $\theta = 0^\circ$ . Our numerical results presented in Fig. 18 agree with these expectations.

Moreover, the deformation of the target nucleus is expected to influence the ratio  $U_{nE\delta}/U_{nEf}$  less and less as the distance between the nuclear surfaces becomes larger. Our results are in accordance with this expectation except at the largest value of  $R$  at which our calculations lose accuracy to a certain extent. This does not influence the fusion barrier, since at such large values of  $R$  the nuclear part of the potential itself is negligibly small in comparison with the Coulomb part. We are unable to explain the irregular scattering of some points corresponding to results of Ref. [11]. However, their results rather often agree well with our calculations.

The  $D(E_{c.m.})$  for the  $^{16}\text{O} + ^{154}\text{Sm}$  reaction calculated using the DFM potential in Ref. [11] revealed a double-peaked structure at the collision energies below the average barrier (see Fig. 6 of that work). No such structure has been found in our calculations, neither for this reaction nor for the others presented in this work (see Figs. 6 and 7).

- 
- [1] R. G. Stokstad, Y. Eisen, S. Kaplanis, D. Pelte, U. Smilansky, and I. Tserruya, *Phys. Rev. Lett.* **41**, 465 (1978).
- [2] N. Rowley, G. R. Satchler, and P. H. Stelson, *Phys. Lett.* **B254**, 25 (1991).
- [3] J. R. Leigh, N. Rowley, R. C. Lemmon, D. J. Hinde, J. O. Newton, J. X. Wei, J. C. Mein, C. R. Morton, S. Kuyucak, and A. T. Kruppa, *Phys. Rev. C* **47**, R437 (1993).
- [4] J. R. Leigh, M. Dasgupta, D. J. Hinde, J. C. Mein, C. R. Morton, R. C. Lemmon, J. P. Lestone, J. O. Newton, H. Timmers, J. X. Wei, and N. Rowley, *Phys. Rev. C* **52**, 3151 (1995).
- [5] C. R. Morton, A. C. Berriman, R. D. Butt, M. Dasgupta, D. J. Hinde, A. Godley, J. O. Newton, and K. Hagino, *Phys. Rev. C* **64**, 034604 (2001).
- [6] D. J. Hinde, M. Dasgupta, J. R. Leigh, J. C. Mein, C. R. Morton, J. O. Newton, and H. Timmers, *Phys. Rev. C* **53**, 1290 (1996).
- [7] J. C. Mein, D. J. Hinde, M. Dasgupta, J. R. Leigh, J. O. Newton, and H. Timmers, *Phys. Rev. C* **55**, R995 (1997).
- [8] R. Hasse and W. J. Myers, *Geometrical Relationships in Nuclear Physics* (Springer-Verlag, Berlin, 1988).
- [9] I. I. Gontchar, M. Dasgupta, D. J. Hinde, R. D. Butt, and A. Mukherjee, *Phys. Rev. C* **65**, 034610 (2002).
- [10] I. I. Gontchar, D. J. Hinde, M. Dasgupta, and J. O. Newton, *Phys. Rev. C* **69**, 024610 (2004).
- [11] M. Ismail and Kh. A. Ramadan, *J. Phys. G* **26**, 1621 (2000).
- [12] D. T. Khoa, W. von Oertzen, and H. G. Bohlen, *Phys. Rev. C* **49**, 1652 (1994).
- [13] D. T. Khoa and G. R. Satchler, *Nucl. Phys.* **A668**, 3 (2000).
- [14] M. J. Rhoades-Brown, V. E. Oberacker, M. Seiwert, and W. Greiner, *Z. Phys. A* **310**, 287 (1983).
- [15] G. Bertsch, J. Borysowicz, H. McManus, and W. G. Love, *Nucl. Phys.* **A284**, 399 (1977).
- [16] N. Anantaraman, H. Toki, and G. F. Bertsch, *Nucl. Phys.* **A398**, 269 (1983).
- [17] G. R. Satchler and W. G. Love, *Phys. Rep.* **55**, 183 (1979).
- [18] D. T. Khoa and W. von Oertzen, *Phys. Lett.* **B304**, 8 (1993).
- [19] D. T. Khoa, G. R. Satchler, and W. von Oertzen, *Phys. Rev. C* **56**, 954 (1997).
- [20] J. W. Negele and D. Vautherin, *Phys. Rev. C* **5**, 1472 (1972).
- [21] X. Campi and A. Bouyssy, *Phys. Lett.* **B73**, 263 (1978).
- [22] D. T. Khoa, *Phys. Rev. C* **63**, 034007 (2001).
- [23] M. Dasgupta, D. J. Hinde, N. Rowley, and A. M. Stefanini, *Annu. Rev. Nucl. Part. Sci.* **48**, 401 (1998).
- [24] T. Cooper, W. Bertozzi, J. Heisenberg, S. Kowalski, W. Turchinets, C. Williamson, L. Cardman, S. Fivozinsky, J. Lightbody, Jr., and S. Penner, *Phys. Rev. C* **13**, 1083 (1976).
- [25] H. de Vries, C. W. de Jager, and C. de Vries, *At. Data Nucl. Data Tables* **36**, 495 (1987).
- [26] D. Kalinsky, L. S. Cardman, R. Yen, J. R. Legg, and C. K. Bockelman, *Nucl. Phys.* **A216**, 312 (1973).
- [27] D. J. Hinde, unpublished data.
- [28] A. Bohr and B. Mottelson, in *Nuclear Structure. Vol. 2, Nuclear Deformations* (Benjamin, New York, 1974), p. 138.
- [29] M. Rashdan, *J. Phys. G* **22**, 139 (1996).
- [30] J. X. Wei, J. R. Leigh, D. J. Hinde, J. O. Newton, R. C. Lemmon, S. Elfstrom, J. X. Chen, and N. Rowley, *Phys. Rev. Lett.* **67**, 3368 (1991).
- [31] S. Raman, C. H. Malarkey, W. T. Milner, C. W. Nestor, Jr., and P. H. Stelson, *At. Data Nucl. Data Tables* **36**, 1 (1987).
- [32] P. Möller, J. R. Nix, W. D. Myers, and W. J. Swiatecki, *At. Data Nucl. Data Tables* **59**, 185 (1995).
- [33] J. O. Newton, R. D. Butt, M. Dasgupta, D. J. Hinde, I. I. Gontchar, C. R. Morton, and K. Hagino, *Phys. Lett.* **B586**, 219 (2004).